DOI: 10.13009/EUCASS2017-465

7TH EUROPEAN CONFERENCE FOR AERONAUTICS AND AEROSPACE SCIENCES (EUCASS)

DOI: ADD DOINUMBER HERE

Direct numerical simulations of transition control in a swept-wing boundary layer using ring-type plasma actuators

Nima Shahriari, Matthias R. Kollert and Ardeshir Hanifi †
Department of Mechanics, Linné FLOW Centre and Swedish e-Science Research Centre (SeRC),
KTH Royal Institute of Technology, SE-100 44 Stockholm, Sweden
nima@mech.kth.se· mrko@kth.se· hanifi@kth.se
†Corresponding author

Abstract

Application of the ring-type plasma actuators for passive control of laminar-turbulent transition in a swept-wing boundary layer is investigated thorough direct numerical simulations. These actuators induce a wall-normal jet in the boundary layer and can act as virtual roughness elements. The flow configuration resembles experiments of Kim et al.,[10] performed within EU project BUTERFLI. The actuators are modelled by the volume forces computed from the experimentally measured induced velocity filed at the quiescent air condition. The natural surface roughness and unsteady perturbations are also included in the simulations. The interaction of generated vortices by the actuators with these perturbations is investigated in details. It is found that for a successful transition control the power of the actuator should be increased to generate a jet velocity one order of magnitude higher than that in the considered experiments.

1. Introduction

Turbulent friction drag on swept wings of modern aircraft accounts for a large proportion of the total drag.[23] Thus, it is desirable to delay transition from laminar to turbulent flow for both environmental and economical reasons. In swept-wing flows, the so called crossflow instability typically dominants the transition process. This instability leads to growth of both streamwise orientated steady and travelling crossflow vortices depending on the external disturbance environment (see reviews by Bippes[1] and Saric et al.[20]). Non-stationary disturbances may dominate the route to transition in environments with rather high levels of freestream turbulence, e.g. wind tunnels. At free-flight cruise conditions, characterised by rather low levels of freestream turbulence, steady crossflow vortices excited by natural surface roughness prevail. Irrespective of the disturbance environment, crossflow vortices generate localised high-shear layers which trigger strong secondary instabilities prior to transition.[25,26]

Several approaches to control transition in boundary-layer flows have been proposed in the literature. The review by Saric et al.[19] summarises the main passive laminar-flow control techniques for swept-wing boundary layers. An encouraging method to control crossflow instabilities is the application of spanwise-periodic distributed micron-sized roughness (DMSR) elements placed near the leading edge of the swept wing. Such elements spaced narrower than the spanwise wavelength of the naturally most amplified mode, excite steady subcritical mode, commonly called the 'control' mode, and induce a useful mean-flow distortion. As a consequence, the growth of the naturally most unstable mode is attenuated and transition to turbulence is delayed. The application of DMSR elements for transition delay have been successfully shown in wind tunnel experiments,[8,21] free-flight experiment[3] and numerically confirmed through direct numerical simulations (DNS)[6,18] and through nonlinear parabolised stability equations (PSE).[13,16]

In a recent experimental investigation,[10] studied the application of ring-type DBD plasma actuators, acting as virtual roughness elements, for transition delay on a swept-wing boundary layer. The ring-type plasma actuators generate a wall-normal jet while the afformentioned works were based on actuators inducing a wall-parallel jet.[10] used rows of actuators with different spanwise spacing and chordwise locations. They observed that the actuators successfully excite the modes corresponding to their spanwise wavelength. However, they were not effective for transition delay and in some actuator configurations transition was promoted by 1.5% chord-length.

This study aims to numerically investigate the experiment of Kim et al.[10] in order to gain a better understanding of the transition process and the role of plasma actuators. First, we study the effect of plasma actuators on the evolution of the primary steady crossflow modes. Then, unsteady disturbances are introduced in the simulations and the evolution of the primary and secondary modes is studied with and without active plasma actuators.

DOI: 10.13009/EUCASS2017-465

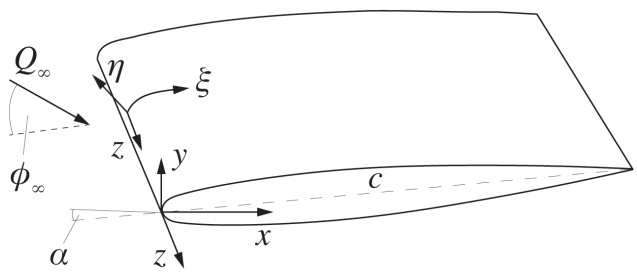

Figure 1: Swept ONERA-D airfoil with sweep angle ϕ_∞ and the total incoming velocity of Q_∞. (x, y, z) and (ξ, η, z) denote the cartesian and the curvilinear coordinate systems respectively. c denotes the chord length normal to the leading edge. The wing is under an angle of attack $\alpha = -8°$.

2. Flow configuration & numerical setup

The wing geometry used in the present investigation is a swept ONERA-D airfoil with a chord length of $c = 0.35m$ normal to the leading edge. The geometry is invariant in the spanwise direction. The flow configuration follows experiments by,[10] performed within the European project BUTERFLI in ONERA TRIN1 wind tunnel, where a sweep angle $\phi_\infty = 60°$ and an angle of attack $\alpha = -8°$ has been used. The unit Reynolds number is $Re_L = Q_\infty L/\nu = 4.4 \times 10^6$, with $L = 1m$ being the reference length scale, $Q_\infty = 70m/s$ the total incoming freestream velocity and ν the kinematic viscosity. Q_∞ is used to normalise velocities in this work. The ring-type plasma actuators with spanwise spacing of $L_{pa} = 3.5mm$ and diameter $d_{pa} = 1mm$ are placed in the leading-edge region of the swept wing at the chordwise location of $x/c = 0.019$ in the experiments. This location is too close to the stagnation point, $x/c = 0.013$, and does not allow for introduction of stationary and non-stationary disturbances upstream of the actuators in the numerical setup. Therefore, center of the actuators are shifted to the chordwise location of $x/c = 0.05$ which is slightly downstream of the neutral point of stationary crossflow modes. Boundary layer is more receptive to the plasma actuators at this location, thus, increasing the effect of the actuators on the evolution of the disturbances.

Figure 1 shows the airfoil shape and the coordinate systems used in this study. The Cartesian coordinates (x, y, z) denote the chordwise, normal-to-the-chord and spanwise directions and the corresponding velocity components are denoted as (u, v, w). The body-fitted curvilinear coordinates (ξ, η, z) define the tangential, wall-normal and spanwise directions with the corresponding velocity components denoted as (u_ξ, v_η, w).

2.1 Direct numerical simulations

We consider incompressible Navier-Stokes equations subject to constant fluid properties together with the continuity equation,

$$\frac{\partial \mathbf{u}}{\partial t} = -\mathbf{u} \cdot \nabla \mathbf{u} - \nabla p + \frac{1}{Re} \nabla^2 \mathbf{u} + \mathbf{f}, \quad \nabla \cdot \mathbf{u} = 0, \tag{1}$$

where $\mathbf{u} = \{u, v, w\}^T$ is the vector of velocity components in the x- ,y- and z- directions, p represents the pressure and $\mathbf{f}$ is the body force term. Equations (1) are integrated in time using `Nek5000` code developed by Fischer et al.[4] `Nek5000` is based on spectral element method (SEM) proposed by[17] which combines geometric flexibility of finite element method with spectral accuracy. The physical domain in SEM is decomposed into spectral elements where the local approximation of flow field is obtained as a sum of Lagrange interpolants defined by an orthogonal basis of Legendre polynomials up to degree N. Polynomial order N is the same in all spatial directions. Following the $\mathbb{P}_N$–$\mathbb{P}_{N-2}$ spatial discretisation[14] , $N + 1$ Gauss-Lobatto-Legendre (GLL) nodes are used to build velocity Lagrange polynomial interpolants and $N - 1$ Gauss-Legendre (GL) nodes for pressure Lagrange polynomial interpolants (two orders less than the velocity field) in every spectral element. Here we have used $N = 11$ for most of the simulations. The equations are advanced in time using a third-order conditionally stable backward differentiation and extrapolation scheme (BDFk/EXTk), employing an implicit treatment of the diffusion term and explicit treatment of the advection term. `Nek5000` is highly parallelised and scalable on thousands of threads.[24] Current results are obtained using up to 4096 processors.

Several sets of simulations have been carried out in this work; (I) laminar base flow is computed through a two-dimensional simulation in which the spanwise velocity component is computed using the temperature equation, (II) steady crossflow vortices are excited by means of natural surface roughness, (III) natural transition is triggered by introducing non-stationary perturbations inside the boundary layer, and (IV) change of transition location due to the action of distributed ring-type plasma actuators is studied.

DOI: 10.13009/EUCASS2017-465

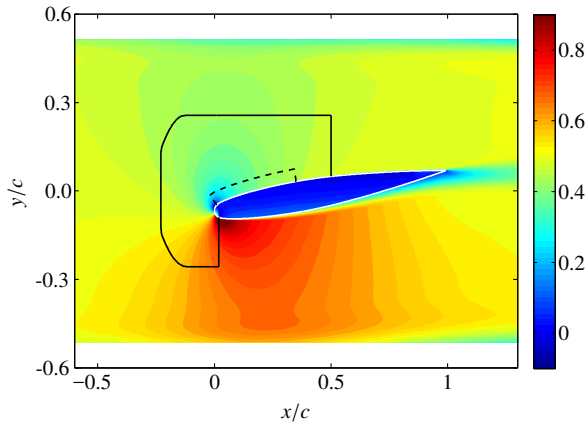

Figure 2: Pseudocolors of streamwise velocity component obtained from RANS solution of the entire wind tunnel test section. The black solid and dashed lines show boundaries of the DNS domain for laminar base flow and receptivity computations, respectively.

2.2 Computational domain & boundary conditions

Prior to performing DNS computations, a complementary RANS solution is obtained around the same geometry with identical flow configuration, depicted in figure 2. The computational domain in the RANS computation includes the side walls of the experimental test section. Two different numerical domains are used in the DNS computations, the boundaries of which are shown in figure 2. The larger domain with two outflow boundaries is used for the laminar base flow computation. Although we are only interested in the flow field on the upper wing side, base flow domain extends to the lower wing side to account for the asymmetry of the configuration. The lower wing part and the leading edge region are discarded in the simulations of the perturbed flow which are performed in the smaller domain plotted with dashed line in figure 2. This is possible since the disturbances are introduced locally within the boundary layer and freestream disturbances, such as sound waves or freestream turbulence, are absent. The inflow and freestream boundary conditions of the perturbed flow are of Dirichlet type and taken from the laminar base flow solution. The outflow boundary conditions are the natural boundary conditions ($[1/Re(\nabla\mathbf{u}) - p\mathbf{I}]\cdot\mathbf{n} = 0$) derived from the weak form of the Navier-Stokes equations. The boundary conditions for the base flow computation are described in the following. Dirichlet boundary conditions are set at the inflow plane using the RANS solution

$$\{u, v, w\}^T = \{u_{\text{rans}}, v_{\text{rans}}, w_{\text{rans}}\}^T \qquad \text{on } \partial\Omega_{\text{inflow}}. \tag{2}$$

The outflow boundary conditions are a modified version of the natural boundary conditions

$$\frac{1}{Re}\frac{\partial u}{\partial x} - p = -p_a, \quad \frac{\partial v}{\partial x} = 0, \quad \frac{\partial w}{\partial x} = 0 \qquad \text{on } \partial\Omega_{\text{outflow}}. \tag{3}$$

Here, p_a stands for the ambient pressure and $p_a = 0$ results to the standard natural boundary conditions which is used in the perturbed flow simulations. The freestream boundary conditions are of Dirichlet type in the streamwise and spanwise directions along with the modified natural condition normal to the surface

$$u = u_{\text{rans}}, \quad \frac{1}{Re}\frac{\partial v}{\partial y} - p = p_a, \quad w = w_{\text{rans}} \qquad \text{on } \partial\Omega_{\text{free-stream}}. \tag{4}$$

The ambient pressure at the free stream is set to $p_a = p_{\text{rans}} - Re^{-1}\partial_y v_{\text{rans}}$ to account for the non-zero pressure gradient around the wing. In all the simulations except the base flow computation, sponge regions are inserted in the vicinity of the outflow boundaries to avoid numerical instabilities.

The base flow domain extends from $x/c = 0.018$ on the lower side of the wing to $x/c = 0.5$ on the upper wing side. The domain for receptivity computations extends from $x/c = 0.01 - 0.35$ on the upper wing side. The 2D mesh for the base flow and the receptivity computations consists of 6300 and 6210 spectral elements respectively.

In the experiments by Kim et al.,[10] an spanwise array of ring-type plasma actuators is inserted near the leading edge of the swept wing as a passive control mechanism to delay transition. The spacing between the actuators is $L_{pa} = 3.5mm$ which corresponds to approximately 2/3 of the wavelength of the naturally most unstable stationary crossflow mode.[6,21] In order to excite the most unstable stationary mode and the control mode (induced by wall-normal jet of the plasma actuators) simultaneously, a spanwise length of $L_z = 3 \times 3.5 = 10.5mm$ is considered which

DOI: 10.13009/EUCASS2017-465

dictates a fundamental spanwise wavenumber $\beta_0 = 2\pi/L_z = 598 rad/m$. We mimic the actuator row by prescribing spanwise periodic boundary conditions. 36 spectral elements are uniformly distributed in the spanwise direction to resolve a span of length L_z. The total number of three-dimensional spectral elements amounts to 223560 and using a polynomial order of $N = 11$ for the velocities results to $\approx 386 \times 10^6$ grid points.

2.3 Stationary perturbations

In the experimental studies, stationary crossflow vortices including the naturally most unstable one are excited due to the presence of the natural surface roughness in the leading edge region of the wing. In this work, the natural surface roughness which is localised along the chord and periodic in the spanwise direction is modelled by

$$h(x, z) = \varepsilon_h h_x(x) h_z(z), \tag{5}$$

where ε_h is the maximum amplitude of the roughness bump and $h_x(x)$ and $h_z(z)$ are shape functions in the streamwise and spanwise directions. The shape function $h_x(x)$ is described by

$$h_x(x) = S\left(\frac{x - h_s}{h_r}\right) - S\left(\frac{x - h_e}{h_f} + 1\right), \tag{6}$$

where S is a smooth step function defined in Schrader et al.[22] The roughness bump in the streamwise direction starts at $x = h_s$, rises smoothly along the distance h_r and ends at $x = h_e$ with a falling distance of h_f. The center of the roughness is located at $x_r = (h_s + h_e)/2$. This shape of roughness contains a broad spectrum of streamwise wavenumbers including the unstable ones. In this study, the natural surface roughness is centred at $x/c = 0.015$ with a total width of $1mm$. The rise and falling distances are equal and set to $h_r = h_f = 0.2mm$. The spanwise periodic shape function $h_z(z)$ is defined as

$$h_z(z) = \sum_{n=1}^{5} \sin(n\beta_0 z + \phi_n^{\text{rand}}), \tag{7}$$

where ϕ_n^{rand} are random phases and $\beta_0 = 2\pi/L_z$ with $L_z = 10.5mm$.

The natural surface roughness is not meshed but modelled by inhomogeneous boundary conditions at the wall. The no-slip conditions along the roughness $h(x, z)$ are projected from the bump surface to the wall via a Taylor series expansion,

$$\{u, v, w\}^T_{wall} = \{-h(x, z)\frac{\partial U}{\partial y}, 0, -h(x, z)\frac{\partial W}{\partial y}\}^T_{wall}, \quad h_s \le x \le h_e, \tag{8}$$

where U and W are the laminar base flow velocities. Since the roughness height ε_h is assumed to be small, the Taylor series is truncated at the first order. The roughness height ε_h is chosen such that the r.m.s. value of the $h(x, z)$ at the roughness centre is matching the reported r.m.s. roughness height of $1\mu m$ in the experiment.

2.4 Non-stationary perturbations

The growth of unsteady instabilities, both primary and secondary, requires the presence of unsteady disturbances such as acoustic noise or freestream turbulence. In this study, non-stationary perturbations are artificially induced inside the boundary layer by employing a weak randomly pulsed volume force. The forcing acts only in the wall-normal direction and reproduces the same effect that tripping strips have in wind-tunnel experiments. The forcing is located downstream of the natural surface roughness at $x/c = 0.024$ and its shape is attenuated by a Gaussian in the streamwise and wall-normal directions. The specific form of the forcing is given in Hosseini et al.[7] The spectral content of the forcing is defined by two parameters, the temporal and the spanwise cut-off scales. The temporal cut-off scale corresponds to an angular frequency of $\approx$ 7000Hz and the spanwise cut-off scale corresponds to $30\beta_0$. The amplitude of the forcing is chosen such that the transition is obtained at $\sim$ 20% chord, similar to the transition location observed in the experiments.

2.5 Plasma actuator body-force field

The ring-type DBD plasma actuator produces a wall-normal jet in the experiments which acts as a virtual roughness element. The action of the actuators in the numerical simulations is incorporated by a body force which corresponds to the velocity field produced by an actuator in quiescent air. Such a velocity field is provided by[9] who placed an actuator sheet on a flat plate and measured the induced velocity field by the actuators in quiescent air. The actuators were

DOI: 10.13009/EUCASS2017-465

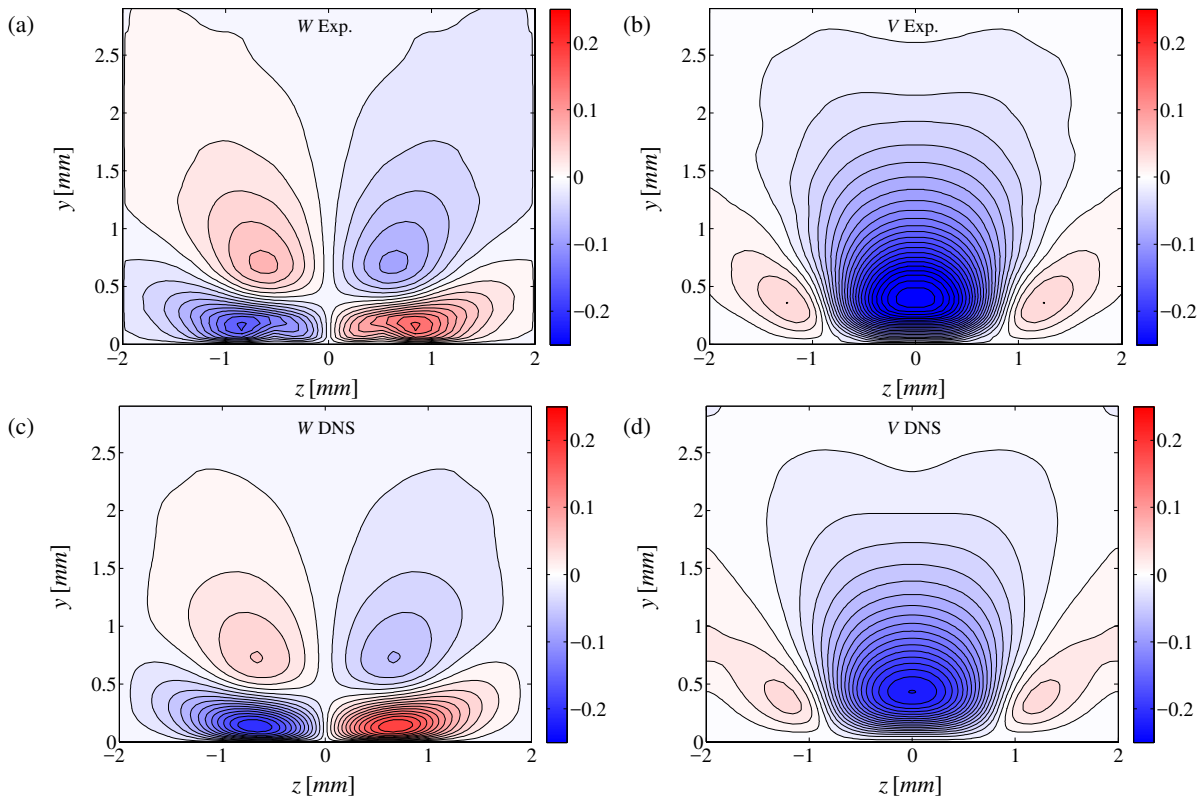

Figure 3: Radial and wall-normal velocity components from experiments (a,b) and computed ones (c,d). All the planes are at $x = 0$. 32 equispaced contours in the range $[-0.25, 0.25]$ and $[-0.3, 0.1]$ are shown for the radial and wall-normal velocity components, respectively.

active under 5.8 kV power supply and at 40 kHz frequency. The measured velocity field is averaged in time and space which results to a steady body force in the numerical simulations. For a ring-type plasma actuator the induced velocity field is symmetric in the radial direction around the center of the actuator. Figure 3(a,b) shows the experimental radial and wall-normal velocity fields induced by the ring-type plasma actuator. In this section, velocity and body force are presented in dimensional values.

`Nek5000` is used to calculate the body force from experimentally measured velocity field induced by a ring-type plasma actuator in quiescent air. The steady body force can be obtained by evaluating

$$-\mathbf{f} = -\mathbf{u} \cdot \nabla \mathbf{u} - \nabla p + \frac{1}{Re} \nabla^2 \mathbf{u}, \tag{9}$$

where $\mathbf{u}$ and p are the experimental velocity and pressure fields. Figure 3(a,b) shows the experimental radial and wall-normal velocity components in the wall-normal spanwise plane at $x = 0$. The computed force field is validated by performing a simulation in quiescent air and comparing the induced velocity field by the body force with the original velocity field. Figure 3(c,d) shows the steady state solution resulting from the plasma actuator body force in quiescent air.

3. Results

3.1 Effect of control on stationary disturbances

In this section we investigate the control capability of ring-type plasma actuator by studying its effect on primary stationary crossflow disturbances. To this end, two setups are considered. In the first setup, stationary crossflow vortices are excited by means of natural surface roughness only and in the second case, plasma actuator body force is activated in the presence of natural surface roughness. In the following these two cases are referred to as the 'natural' and the 'controlled' case respectively.

DOI: 10.13009/EUCASS2017-465

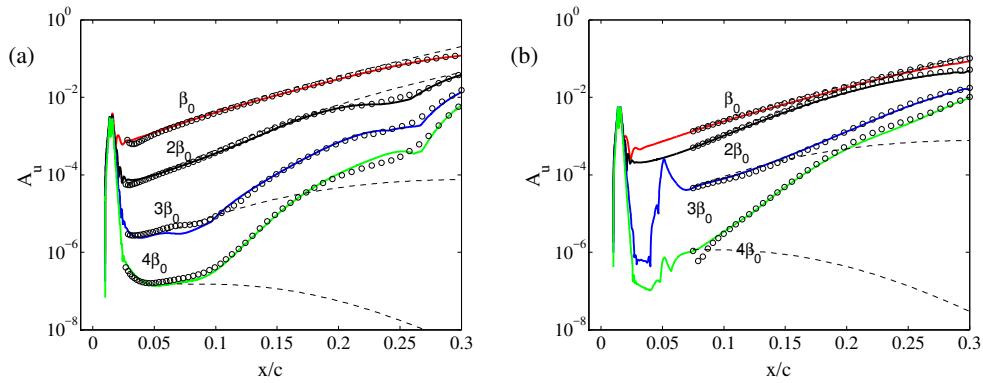

Figure 4: Amplitude evolution A_u of the stationary modes for (a) natural and (b) controlled case in the absence of unsteady perturbations. Solid lines represent DNS amplitudes, dashed lines and (∘) symbols show the amplitude evolution predicted by linear and nonlinear PSE respectively.

In order to compare the natural and the controlled case quantitatively, amplitude of individual crossflow modes is obtained by means of Fourier transformation in the spanwise direction, i.e.

$$u_\xi(\xi,\eta,z) = \sum_{n=0}^{N} \hat{u}_\xi(\xi,\eta,n\beta_0)e^{in\beta_0 z}. \tag{10}$$

Here, $\beta_0 = 2\pi/L_z$ is the fundamental spanwise wavenumber dictated by the spanwise length of the domain. Amplitudes of individual modes for both the natural and the controlled case are plotted in figure 4 as

$$A_u(x) = \max_\eta \frac{|\hat{u}_\xi|}{Q_\infty}, \tag{11}$$

where, $\hat{u}_\xi$ is the Fourier amplitude of the tangential velocity and Q_∞ denotes the total freestream velocity. Linear stability analysis of the underlying base flow predicts that the most unstable stationary crossflow mode is the $2\beta_0$ mode. However, for both cases, amplitude of the fundamental β_0 mode dominates the amplitude of its superharmonics. Although all the excited modes by natural surface roughness have identical amplitudes at the roughness location, the fundamental mode is the most receptive to the surface roughness. This is due to the fact that the neutral point of stationary modes is located around $x/c \approx 0.04$ and the surface roughness is positioned upstream of this location at $x/c = 0.015$. Therefore, the modes excited by the natural roughness first decay in amplitude, with different decay rates, until they reach their corresponding neutral point and then grow and evolve moving downstream. The growth rate (slope of the amplitude curve) of the $2\beta_0$ mode is however larger than the fundamental mode, conforming the linear stability prediction.

Figure 4 also shows the amplitude evolution of different modes obtained by linear and nonlinear PSE computations on the underlying base flow. The initial amplitude of modes for nonlinear PSE computations are extracted from DNS solutions at $x/c = 0.03$ and $x/c = 0.075$ for the natural and controlled case respectively. Despite slight discrepancies between nonlinear PSE and DNS, the overall agreement is found to be very good. For both natural and control cases, the β_0 mode shows linear growth up to $x/c \approx 0.25$ and the $2\beta_0$ mode behaves linearly up to the chord length $x/c \approx 0.20$. No nonlinear amplitude saturation is observed through the computational domain.

3.2 Unsteady disturbances and secondary instabilities

In the previous section we showed the effect of control on evolution of primary stationary crossflow disturbances in the absence of unsteady perturbations. Because of the high accuracy of the DNS code, there were no background noise in the simulations, thus, flow did not transition to turbulence. In this section a more realistic setup is considered. Unsteady perturbations are introduced in the boundary layer by means of random volume force described in section §2.4. The amplitude of the random force is chosen such that transition is obtained close to the experimental transition location. Similar to the previous section, we study a natural and a controlled case. In the former setup, steady crossflow disturbances are excited by the surface roughness model while unsteady disturbances are introduced by employing random volume force. In the controlled case, plasma actuator body force is added to the natural setup in order to excite the steady control mode.

DOI: 10.13009/EUCASS2017-465

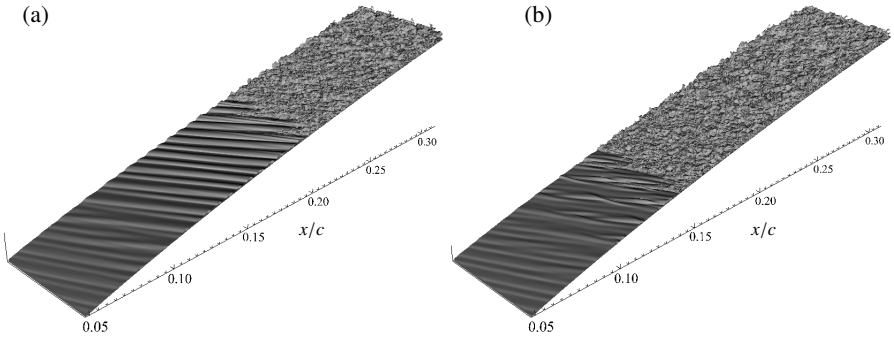

Figure 5: Isosurfaces of instantaneous spanwise velocity field (a) natural and (b) controlled case. For better visualisation, domain is duplicated in the spanwise direction.

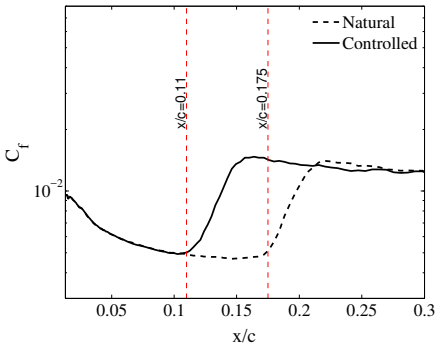

Figure 6: Time averaged friction coefficient for the natural and the controlled case.

Figure 5 shows isosurfaces of instantaneous spanwise velocity for both the natural and the controlled case. Similar to the experimental observations, it is apparent that employing the control by plasma actuators have promoted transition. A quantitative measure for transition location is obtained by evaluating wall-friction coefficient. A breakdown to turbulent flow is accompanied by a strong increase in this coefficient. Figure 6 shows time-averaged friction coefficient $C_f = 2\mu(\partial u_s/\partial\eta)$ for both the natural and the controlled case where $u_s = u_\xi \cos(\phi_\infty) + w \sin(\phi_\infty)$ is the velocity in the direction of incoming free-stream. The time averaging is required due to unsteadiness of the transition location for both cases (±3% chord-length). In the natural case, transition starts at $x/c \approx 0.175$ with appearance of turbulent spots and flow becomes fully turbulent at $x/c \approx 0.22$. In the controlled case, transition location moves upstream to $x/c \approx 0.11$, with a fully turbulent flow at $x/c \approx 0.16$.

In order to characterise the disturbance environment and the transition mechanism, the total velocity filed is decomposed into time-periodic Fourier modes. This will allow us to capture the evolution of both steady and unsteady perturbations. Additionally, the onset of secondary instabilities can be identified by an explosive growth of high-

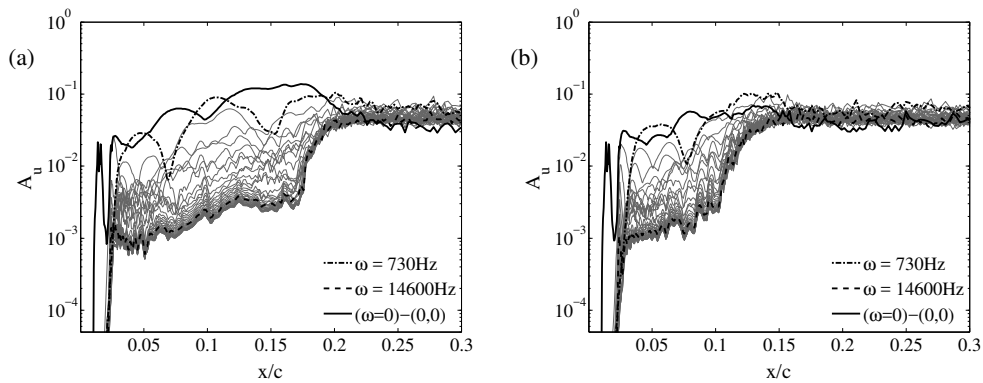

Figure 7: Amplitude evolution of steady and unsteady disturbances for (a) natural case and (b) controlled case. The gray lines represent unsteady disturbances plotted at a constant frequency step of 730Hz.

DOI: 10.13009/EUCASS2017-465

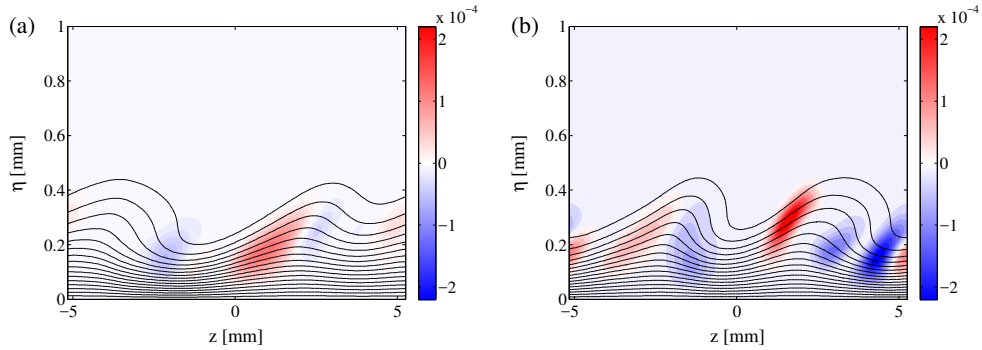

Figure 8: Contours of modified mean flow (tangential component) in black and distribution of the production term $-\tilde{u}_\xi \tilde{w} \partial U_\xi / \partial z$ for the high-frequency mode with frequency 14600Hz. (a) natural case and (b) controlled case. The wall-normal plane is chosen at $x/c = 0.09$, located upstream of the transition location in both cases. Contour levels are identical in both cases.

frequency modes similar to the observations in previous studies.[6,16,25–27] To this end, amplitude of individual crossflow modes is obtained by means of Fourier transformation in time, i.e.

$$u_\xi(\xi, \eta, z, t) = \sum_{m=0}^{M} \tilde{u}_\xi(\xi, \eta, z, m\omega_0) e^{im\omega_0 t}. \tag{12}$$

Amplitudes of individual modes for both the natural and the controlled case are plotted in figure 7 as

$$A_u(x) = \max_{\eta,z} \frac{|\tilde{u}_\xi|}{Q_\infty}, \tag{13}$$

where, $\tilde{u}_\xi$ is the time Fourier amplitude of the tangential velocity and Q_∞ denotes the total freestream velocity. Amplitude of steady disturbances is obtained by subtracting the mean flow, i.e. the (0,0)-mode, from the zero-frequency mode. Owing to the complexity of the set up, the amplitude evolution of disturbances is rather complicated. Both steady and unsteady disturbances grow throughout the domain. The amplitude of steady and low-frequency disturbances are of similar order and in the controlled case, low-frequency disturbances exhibit even higher amplitudes than the stationary disturbances. Complimentary linear PSE computations suggests that the most unstable crossflow disturbance has angular frequency of $\omega \approx 800$Hz and spanwise wavelength of $\beta \approx 7mm$. Therefore, the low-frequency disturbances can be associated with unsteady primary crossflow disturbances.

In both cases, high-frequency disturbances are excited and just upstream of the transition location they undergo sudden amplification and reach the amplitude of primary modes within few percent chord length. This is a characteristic behaviour of secondary instabilities; once the primary crossflow waves reach high amplitudes, secondary instabilities are destabilised and grow to large amplitudes over a very short streamwise distance and lead to breakdown and turbulence.[27] Here, the amplitudes of primary disturbances, both the steady and unsteady ones, reach $\sim 10\%$ of the total freestream velocity prior to transition. Due to complex disturbance environment in our setup, it is not easy to isolate the secondary instability mechanism. Under more controlled conditions, it has been shown that transition is induced either by stationary or travelling saturated crossflow disturbances.[5,16,25,26] Moreover, in works by Lerche and Bippes[11,12] it was observed that a superposition of both stationary and travelling primary modes can destabilise the secondary instability, while individually they are not strong enough to produce sufficient mean-flow deformation and trigger the secondary instability. In this case, transition is induced by co-existing steady and unsteady crossflow disturbances which exhibit similar amplitudes.

Based on disturbance energy production, secondary instabilities are often categorised into two types;[15,16] z- and y-type modes that are produced by the spanwise and wall-normal gradients of the mean streamwise velocity, respectively. Figure 8 shows streamwise velocity component of the modified mean flow along with the distribution of the energy production term associated with a z-type mode, $-\tilde{u}_\xi \tilde{w} \partial U_\xi / \partial z$, for the high-frequency mode with frequency 14600Hz. The sign of the production term indicates whether the local transfer of kinetic energy associated with it acts as stabilising (negative) or destabilising (positive). The wall-normal plane (η, z) is chosen at $x/c = 0.09$, an upstream position of the transition location for both natural and controlled cases. Although, the crossflow vortices are not saturated in either case, the mean-flow modification by the control mode has resulted in formation of stronger crossflow vortices. The maximum of the production is located on the updraught side of the primary vortices with slightly larger values in the controlled case. Therefore, the secondary instabilities are destabilised earlier than the uncontrolled case which is followed by promotion of transition to turbulence.

DOI: 10.13009/EUCASS2017-465

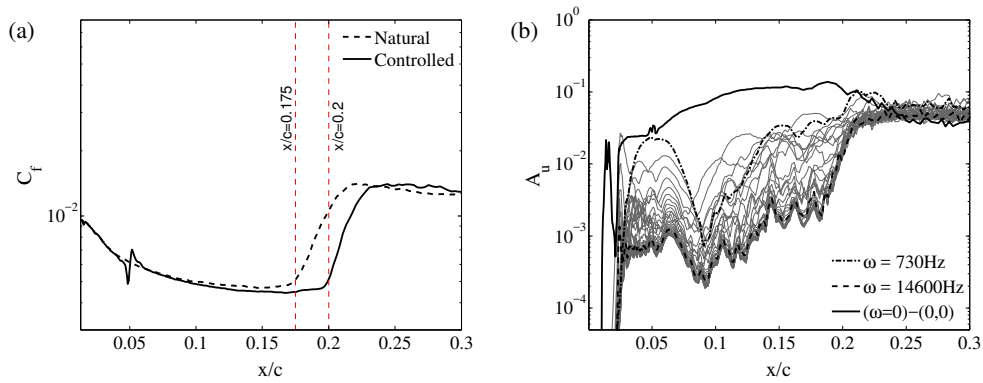

Figure 9: (a) Time averaged friction coefficient for the natural and the improved controlled case. (b) Amplitude evolution of steady and unsteady disturbances for the improved controlled case with higher plasma actuator body force. The gray lines represent unsteady disturbances plotted at a constant frequency step of 730Hz.

3.3 Improved control & transition delay

In this section we aim to improve the control and delay transition using ring-type plasma actuators investigate here. There are several design parameters in this control technique which could be investigated for improvement, i.e. the streamwise location or the spanwise spacing of plasma actuators and the strength of actuators in terms of magnitude of the induced velocity (which corresponds to the height of a roughness element). Actuators should be located at streamwise locations where the boundary layer is more receptive to the excitation of the control mode. Here we have positioned the actuators slightly downstream of the neutral point of the stationary crossflow vortices. The spanwise spacing of the actuators is chosen smaller than the spanwise wavelength of the naturally most unstable mode so that the control mode is subcritical with respect to the most amplified mode and decays far downstream. Following the suggestion by,[21] we have spaced the plasma actuators with a spanwise wavelength equal to $2/3$ of the wavelength of naturally most unstable mode.[3] placed roughness elements at $1/2$ of the wavelength of the most unstable crossflow mode in their free-flight experiments which was found to be effective in delaying transition. Choosing higher harmonics of the most unstable mode is also possible but the control mode may become too damped and therefore not effective.

In the successful applications of this control technique, Wassermann and Kloker,[25] and Hosseini et al.[6] have shown the amplitude of control mode is around one order of magnitude larger than the most unstable stationary mode in the upstream regions of their flow cases (e.g. see figure 3 of the latter study). Furthermore, Wassermann and Kloke[25] show that increasing the amplitude of control mode results in further suppression of the most unstable stationary modes and hence a more effective control (e.g. see their figure 24). Moreover, suppression of unsteady disturbances by nonlinear steady crossflow modes have been shown by Bonfigli and Kloker.[2] In our flow case, the amplitude of control mode, shown in figure 4(b), is one order of magnitude smaller than the amplitude of the most unstable mode and it is too weak compared to the cases in which the control have successfully delayed transition. Therefore, among the design parameters mentioned, we choose to investigate the plasma actuator strength for improvement of the control. To this end, plasma actuator body force is increased by a factor of 100 which corresponds to increasing the magnitude of the induced jet velocity by one order of magnitude from $\approx 0.2m/s$ to $\approx 5.0m/s$.

In order to evaluate the control capability of the plasma actuators with stronger body force in a realistic more complex disturbance environment, unsteady perturbations are introduced in the domain. Figure 9(a) shows the time-averaged friction coefficient for both the natural and the controlled case. It is clear that the new control has delayed transition to turbulent flow by about 3% chord-length. Fourier transform of flow field snapshots in time, characterises the disturbance environment into steady and unsteady parts. Amplitude of the individual modes, as defined in equation (13), for the controlled case are plotted in figure 9(b). The steady disturbances are clearly dominant in this controlled case. The initial amplitude of unsteady perturbations, both primary and secondary, are similar to the uncontrolled case up to the location of plasma actuators at $x/c = 0.05$. Thereafter, they experience a sharp decay up to $x/c \approx 0.1$ where they start to grow again. However, the unsteady disturbances are attenuated compared to the natural case. Furthermore, the sudden growth of high-frequency disturbances is shifted downstream which corresponds to the beginning of the transition location in the friction coefficient curve.

In order to understand further the mechanism of secondary instabilities, transfer of energy between the base flow and high-frequency modes is investigated. To this end, spatial distribution of energy production term associated with z-type modes, $-\tilde{u}_\xi \tilde{w} \partial U_\xi / \partial z$, for the high-frequency mode with frequency of 14600Hz along with contours of modified mean flow is shown in figure 10. The wall-normal plane is chosen at $x/c = 0.17$, prior to the transition location in

DOI: 10.13009/EUCASS2017-465

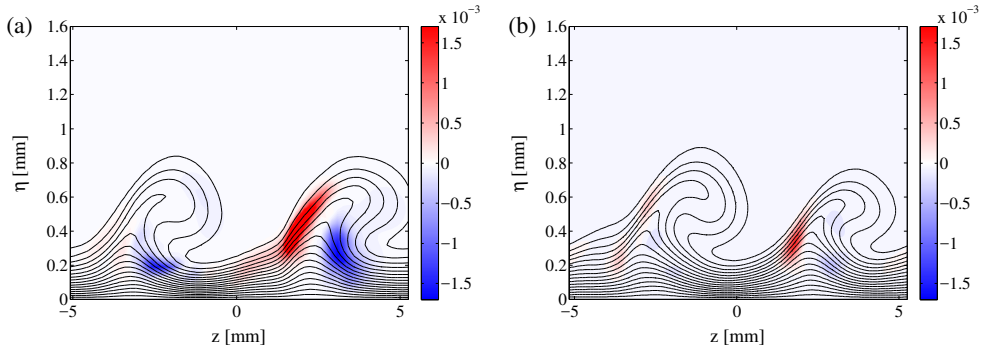

Figure 10: Spatial distribution of the production term $-\tilde{u}_\xi \tilde{w} \partial U_\xi / \partial z$ for the high-frequency mode with frequency 14600Hz along with contours of modified mean flow (tangential velocity component). (a) natural case and (b) controlled case. The wall-normal (η, z) plane is located at $x/c = 0.17$.

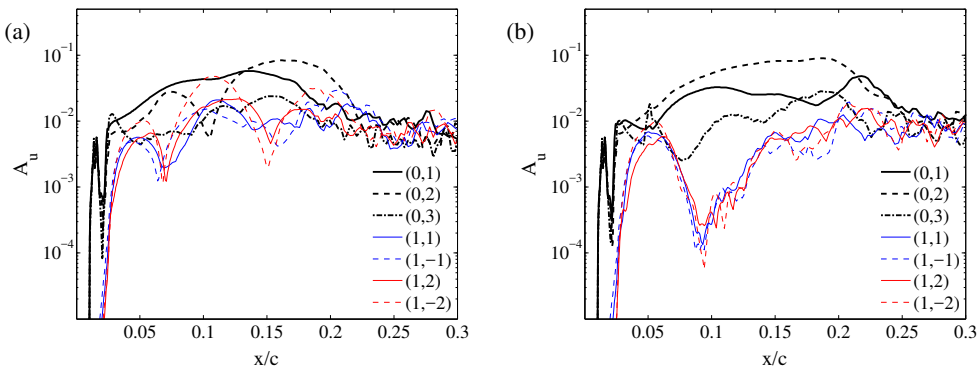

Figure 11: Amplitude evolution of primary modes for (a) natural case and (b) the controlled case, obtained using spatio-temporal Fourier decomposition of disturbances.

both controlled and uncontrolled cases. The maximum production is located on the upwelling zone of the stationary crossflow vortices where the shear is strong. The destabilising energy production is clearly weaker in the controlled case as compared with the natural case. Although figure **??**(a) shows dominance of the control mode in the absence of unsteady disturbances, the mean flow structure in both natural and controlled cases is dominated by the most unstable $2\beta_0$ mode in the presence of unsteady perturbations. In order to investigate this behaviour, disturbances are assumed to be spanwise- and time-periodic and may be decomposed into Fourier components of the form

$$u_\xi(\xi, \eta, z, t) = \sum_{m=0}^{M} \sum_{n=-N}^{N} \tilde{u}_\xi(\xi, \eta, n\beta_0, m\omega_0) e^{i(n\beta_0 z + m\omega_0 t)}. \tag{14}$$

Amplitudes of individual modes for both the natural and the controlled case are plotted in figure 11 as

$$A_u(x) = \max_\eta \frac{|\tilde{u}_\xi|}{Q_\infty}. \tag{15}$$

In the following individual Fourier modes with a spanwise wavenumber $n\beta_0$ and a frequency $m\omega_0$ are represented by (m, n). The fundamental frequency resolved here is 730Hz. In the natural case, steady and unsteady disturbances exhibit similar amplitude levels with the (0,1)-mode being dominant up to $x/c \approx 0.13$ where the (0,2)-mode becomes dominant. In the controlled case, excitation of the control mode clearly attenuates the unsteady modes as well as the (0,1)-mode. The dominant mode throughout the domain is the (0,2)-mode in contrast to dominance of the control (0,3)-mode in purely steady disturbance environment. This demonstrates the significant effect of unsteady disturbances in the receptivity process.

4. Conclusions

Passive control of a swept-wing boundary layer using ring-type plasma actuators is investigated thorough direct numerical simulations. The flow configuration conforms to experiments by Kim et al.,[10] performed within EU project

DOI: 10.13009/EUCASS2017-465

BUTERFLI. Such actuators generate a wall-normal jet and act as virtual roughness elements to excite subcritical stationary control modes. The action of actuators are incorporated in the numerical simulations by including the corresponding body force of the induced velocity field by actuators. Steady crossflow disturbances are excited using a simplified model of natural surface roughness on the wing surface.

First, the effect of control on the evolution of stationary crossflow disturbances in the absence of unsteady perturbations is investigated, i.e. transition is not studied. Excitation of the control mode attenuates the amplitude of most unstable mode as well as the total amplitude of stationary disturbances. The amplitude of dominant mode in both the natural and the controlled case is rather low and not saturated within the computational domain. In the next step, a more realistic disturbance environment is considered by adding unsteady disturbances in the leading edge region using random volume force in the wall-normal direction. The amplitude of unsteady perturbations is adjusted such that the transition location is close to the experimental one. Employing control in this setup leads to promotion of transition which is in qualitative agreement with the experimental observations. The breakdown from laminar to turbulent flow is caused by explosive growth of secondary instability modes. In both the natural and the controlled case, stationary and travelling crossflow modes exhibit similar amplitudes and a combination of both modes triggers the secondary instabilities.

An improvement in the control is demonstrated by employing stronger plasma actuators with one order of magnitude larger jet velocity. In the absence of unsteady perturbations, the amplitude of control mode for such plasma actuator initially dominates the amplitude of the stationary modes and decays far downstream. This behaviour is in qualitative agreement with previous studies.[6,25] It is shown that employing stronger plasma actuators in a disturbance environment with both steady and unsteady perturbations successfully delays transition. Amplitude of unsteady disturbances, both primary and secondary, is attenuated when control is applied. However, the modified mean flow is still dominant by the naturally most unstable crossflow mode. This is confirmed by spatio-temporal Fourier decomposition of disturbances. The results of the simulations show a complex interaction between stationary and unsteady vortices indicating the importance of unsteady crossflow vortices in transition for the case under consideration.

Acknowledgments

The authors would like to thank Philip Dörr for fruitful discussions and valuable comments. This work has been supported by the European commission through FP7 project BUTERFLI (grant agreement no. ACP3-GA-2013-605605). Computer time provided by SNIC (Swedish National Infrastructure for Computing) is gratefully acknowledged.

References

[1] H. Bippes. Basic experiments on transition in three-dimensional boundary layers dominated by crossflow instability. *Prog. Aerospace Sci.*, 35(4):363–412, 1999.

[2] G. Bonfigli and M. Kloker. Spatial navier-stokes simulation of crossflow-induced transition in a three-dimensional boundary layer. In *New Results in Numerical and Experimental Fluid Mechanics II*, pages 61–68. Springer, 1999.

[3] A. L. Carpenter, William S Saric, and Helen L Reed. In-flight receptivity experiments on a 30-degree swept-wing using micron-sized discrete roughness elements. *AIAA paper 2009-590*, 2009.

[4] P. F. Fischer, J. W. Lottes, and S. G. Kerkemeier. Nek5000 Web page, 2008. http://nek5000.mcs.anl.gov.

[5] M. Högberg and D. Henningson. Secondary instability of cross-flow vortices in Falkner-Skan-Cooke boundary layers. *J. Fluid Mech.*, 368:339–357, 1998.

[6] S. M. Hosseini, D. Tempelmann, A. Hanifi, and D. S Henningson. Stabilization of a swept-wing boundary layer by distributed roughness elements. *J. Fluid Mech.*, 718:R1, 2013.

[7] S. M. Hosseini, R. Vinuesa, P. Schlatter, A. Hanifi, and D. S Henningson. Direct numerical simulation of the flow around a wing section at moderate reynolds number. *Int. J. of Heat and Fluid Flow*, 2016.

[8] Y. S. Kachanov, V. I. Borodulin, and A. V. Ivanov. Transition experiments with controlled freestream turbulence level and controlled acoustic pertubations. Technical report, RODTRAC project TR D4.3, 2015.

[9] J.-H. Kim and K.-S. Choi. Report on the properties and operation conditions of the actuators producing a spanwise row of wall-normal jets and the flow induced in the preliminary tests. Technical report, BUTERFLI Project TR D3.15, 2016.

DOI: 10.13009/EUCASS2017-465

[10] J.-H. Kim, M. Forte, and K.-S. Choi. Report on the experimental results on transition delay in the "Juju" TRIN1 wind tunnel by the VR DBD actuators based on wall-normal jets. Technical report, BUTERFLI Project TR D3.19, 2016.

[11] T. Lerche. Experimental investigation of nonlinear wave interactions and secondary instability in three-dimensional boundary-layer flow. In *Advances in Turbulence VI*, pages 357–360. Springer, 1996.

[12] T. Lerche and H. Bippes. Experimental investigation of cross-flow instability under the influence of controlled disturbance excitation. *Transitional Boundary Layers in Aeronautics (ed. RAWM Henkes & JL van Ingen). North Holland*, 1996.

[13] F. Li, M. Choudhari, C.-L. Chang, C. L. Streett, and M. H. Carpenter. Roughness based crossflow transition control: a computational assessment. *AIAA Paper 2009-4105*, 2009.

[14] Y. Maday and A. T. Patera. Spectral element methods for the incompressible Navier–Stokes equations. In *State of the art surveys on computational mechanics. New York, ASME*, volume 1, pages 71–143, 1989.

[15] M. R. Malik, F. Li, and C.-L. Chang. Nonlinear crossflow disturbances and secondary instabilities in swept-wing boundary layers. In *IUTAM Symposium on Nonlinear Instability and Transition in Three-Dimensional Boundary Layers*, pages 257–266. Springer, 1996.

[16] M. R Malik, F. Li, M. M. Choudhari, and C.-L. Chang. Secondary instability of crossflow vortices and swept-wing boundary-layer transition. *J. Fluid Mech.*, 399:85–115, 1999.

[17] A. T. Patera. A spectral element method for fluid dynamics: laminar flow in a channel expansion. *J. comp. Phys.*, 54(3):468–488, 1984.

[18] D. P. Rizzetta, M. R. Visbal, H. L. Reed, and W. S. Saric. Direct numerical simulation of discrete roughness on a swept-wing leading edge. *AIAA J.*, 48(11):2660–2673, 2010.

[19] W. S. Saric, A. L. Carpenter, and H. L. Reed. Passive control of transition in three-dimensional boundary layers, with emphasis on discrete roughness elements. *Phil. Trans. Roy. Soc. Lond. A*, 369(1940):1352–1364, 2011.

[20] W. S Saric, H. L Reed, and E. B White. Stability and transition of three-dimensional boundary layers. *Ann. Rev. Fluid Mech.*, 35(1):413–440, 2003.

[21] W. S. Saric, Jr. R. Carrillo, and M. Reibert. Leading-edge roughness as a transition control mechanism. In *AIAA Paper 98-0781*, 1998.

[22] L.-U. Schrader, L. Brandt, and D. S. Henningson. Receptivity mechanisms in three-dimensional boundary-layer flows. *J. Fluid Mech.*, 618:209–241, 2009.

[23] G. Schrauf. Status and perspectives of laminar flow. *Aeronautical J.*, 109(1102):639–644, 2005.

[24] H. M. Tufo and P. F. Fischer. Fast parallel direct solvers for coarse grid problems. *J. Parallel and Distributed Computing*, 61(2):151–177, 2001.

[25] P. Wassermann and M. Kloker. Mechanisms and passive control of crossflow-vortex-induced transition in a three-dimensional boundary layer. *J. Fluid Mech.*, 456:49–84, 2002.

[26] P. Wassermann and M. Kloker. Transition mechanisms induced by travelling crossflow vortices in a three-dimensional boundary layer. *J. Fluid Mech.*, 483:67–89, 2003.

[27] E. B. White and W. S. Saric. Secondary instability of crossflow vortices. *J. Fluid Mech.*, 525:275–308, 2005.